Petroleum Science 20 (2023) 1546–1561

Contents lists available at ScienceDirect

Petroleum Science

journal homepage: www.keaipublishing.com/en/journals/petroleum-science

Original Paper

Extracting angle-domain common-image gathers in VTI media using ansiotropic-Helmholtz P/S wave-mode decomposition

Le-Le Zhang [a], Yang Zhao [a, *], Lu Liu [b], Ke Chen [a], Jia-Hui Zuo [a], Yi-Xin Wang [a], Ji-Dong Yang [c]

[a] State Key Laboratory of Petroleum Resource and Prospecting, Unconventional Petroleum Research Institute, China University of Petroleum, Beijing, 102249, China
[b] Aramco Beijing Research Center, Aramco Asia, Beijing, 100102, China
[c] Department of Geophysics, China University of Petroleum (East China), Qingdao, Shandong, 266580, China

ARTICLE INFO

Article history:
Received 22 June 2022
Received in revised form
4 November 2022
Accepted 20 February 2023
Available online 26 February 2023

Edited by Jie Hao

Keywords:
Helmholtz decomposition
Angle gathers
Anisotropy
Elastic-RTM

ABSTRACT

Common-image gathers are extensively used in amplitude versus angle (AVA) and migration velocity analysis (MVA). The current state of methods for anisotropic angle gathers extraction use slant-stack, local Fourier transform or low-rank approximation, which requires much computation. Based on an anisotropic-Helmholtz P/S wave-mode decomposition method, we propose a novel and efficient approach to produce angle-domain common-image gathers (ADCIGs) in the elastic reverse time migration (ERTM) of VTI media. To start with, we derive an anisotropic-Helmholtz decomposition operator from the Christoffel equation in VTI media, and use this operator to derive the decomposed formulations for anisotropic P/S waves. Second, we employ the first-order Taylor expansion to calculate the normalized term of decomposed formulations and obtain the anisotropic-Helmholtz decomposition method, which generates the separated P/S wavefields with correct amplitudes and phases. Third, we develop a novel way that uses the anisotropic-Helmholtz decomposition operator to define the polarization angles for anisotropic P/S waves and substitute these angles to decomposing formulations. The polarization angles are then calculated directly from the separated vector P- and S-wavefields and converted to the phase angles. The ADCIGs are thusly produced by applying the phase angles to VTI ERTM. In addition, we develop a concise approximate expression of residual moveout (RMO) for PP-reflections of flat reflectors in VTI media, which avoids the complex transformations between the group angles and the phase angles. The approximate RMO curves show a good agreement with the exact solution and can be used as a tool to assess the migration velocity errors. As demonstrated by two selected examples, our ADCIGs not only produce the correct kinematic responses with regards to different velocity pertubatation, but also generate the reliable amplitude responses versus different angle. The final stacking images of ADCIGs data exhibit the identical imaging effect as that of VTI ERTM.

1. Introduction

Acoustic reverse time migration (ARTM) considers the earth media as fluid medium and only contains the P-wave information. In contrast, elastic reverse time migration (ERTM) can utilize the P-to-S waves and investigate the complex geological structures (Liu, 2019; Granli et al., 1999; Caldwell, 1999; Tang et al., 2009). For anisotropic media, there are no pure P- and S-wave due to that the polarization deviates from propagating direction (except for some special directions). Therefore, we call the anisotropic P- and S-waves as quasi P- (qP-) and quasi S- (qS-) waves (Mu et al., 2020b).

The ERTM workflow includes calculating the source- and receiver-side wavefields, decomposing these wavefields into P- and S-components, and then applying the cross-correlation imaging condition to produce PP- and PS-images. Among these procedures, P/S wave-mode decomposition is a critical step to suppress cross-artifacts (Yang et al., 2019; Qu et al., 2017a; Mu et al., 2020a). In isotropic media, the classical Helmholtz decomposition (Morse and

* Corresponding author.
E-mail address: zhaoyangprof1@qq.com (Y. Zhao).

https://doi.org/10.1016/j.petsci.2023.02.021

Feshbach, 1953) is usually used to separate original wavefields into scalar P-wave potential and vector S-wave potential. This way changes the phases and amplitudes of input wavefields (Duan and Sava, 2015; Wang et al., 2015; Qu et al., 2019). To tackle this problem, Zhang and Mcmechan (2010) simulate correct vector P/S wavefiel using the wavenumber operators. This method needs local homogeneous assumption. Zhu (2017) develops a similar decomposition method in the space domain by introducing a Poisson equation. To improve the efficiency, Yang et al. (2018) and Zhao et al. (2018) avoid the Poisson equaiton via integrating the source and receiver fields. In anisotropic media, however, the wave propagation vector is neither parallel nor orthogonal to the qP- and qS-wave polarization direction (Crampin, 1977). The straightforward approach decouples anisotropic qP- and qS-waves in the wavenumber domain by solving the Christoffel equation (Dellinger and Etgen, 1990; Zhang and Mcmechan, 2010) with a local homogeneous assumption. For a heterogeneous medium, anisotropic P/S wave-mode decomposition can be implemented by applying the non-stationary filtering operators (Yan, 2009), low-rank approximation (Cheng and Fomel, 2014), or LU factorization (Yang et al., 2019). However, these methods require strong model assumption or large computations. Recently, Zhang et al. (2022) develops an anisotropic-Helmholtz decomposition method to efficiently decouple P/S wavefields in the space-wavenumber domain. This approach is feasible for arbitrary heterogeneous models and generates vector qP- and qS-wavefields with correct units, amplitudes, and phases as original wavefields. In this paper, we apply the anisotropic-Helmholtz decomposition method to the P/S wave-mode separation and generate corresponding ADCIGs in VTI ERTM.

The intrinsic anisotropy exists in elastic media due to the dominant orientation of anisotropic mineral grains and the shapes of isotropic minerals (Thomsen, 1986; Tsvankin, 2012). Because the anisotropy is related to wave propagation angle (phase angle), angle-domain common-image gathers (ADCIGs) are critical for anisotropic and elastic parameter inversion (Qu et al., 2017b). For example, ADCIGs are a popular tool for migration velocity analysis (MVA) because the residual moveouts (RMO) in ADCIGs can reflect the velocity errors. Amplitude versus angle (AVA) also requires a high-quality ADCIGs to invert the subsurface lithological feature. ADCIGs are estimated from the incident phase angle of decomposed qP- and qS-wavefields. In isotropic media, the phase angle, polarization angle, and group angle share the same value, since they all represent the wave propagating direction. Popular methods for the ADCIG extraction including Poynting vector (Tang and McMechan, 2018; Wang et al., 2016b), optical flows (Zhang et al., 2018), extended image condition (Yan and Sava, 2008; Vyas et al., 2010), recursive Radon transform (Liu et al., 2016) or polarization direction (Zhang and McMechan, 2011b). However, in anisotropic media, the phase angle, polarization angle, and group angle are inequivalent and related to anisotropic parameters. They may convert to each other but require complex transfer functions (Tsvankin, 2012; Lu et al., 2019). The anisotropic acoustic ADCIGs can be extracted by the space-shift imaging condition in the Fourier domain (Sava and Fomel, 2005) or slant stacks performed on pre-stack images (Biondi, 2007a). Xu et al. (2011) apply 4D Fourier transform (FT) to 3D RTM to produce anisotropic ADCIGs. These methods are implemented on the local Fourier domain and are computationally expensive. The Poynting vector (Lu et al., 2019; Wang and Zhang, 2022) is able to compute group angle which is then converted to polarization and phase angle for ADCIGs extraction. However, this method tends to distort by the interference of complex wavefields and produces inaccurate angles. Zhang and McMechan (2011a) apply the local FT to separated the qP- and qS-wavefields and then use the separated qP-wavefield to calculate the polarization angle for ADCIGs extraction. Wang et al. (2016a) utilizes the low-rank approximation to separate vector qP- and qS-wavefields to obtain the corresponding polarization and phase angles. The angle accuracy and computational cost are heavily depending on the selected rank number. In addition to ADCIGs extraction, the residual moveout (RMO) measurement is also important to evaluate the velocity corrections. There are many RMO studies in isotropic (Biondi and Symes, 2004; Zhang et al., 2012; Zhao et al., 2020) and anisotropic media (Jousselin and Biondi, 2006; Biondi, 2007a, 2007b). For instance, Biondi (2007b) build a quantitative connection between velocity perturbations and the event moveouts in anisotropic ADCIGs. A RMO expression is developed as the function of the phase and group angle. However, the conversion from the group angle to the phase angle is not straightforward and requires expensive computations.

Compared with previous studies, this paper presents three improvements in extracting ADCIGs of ERTM in VTI media. 1) P/S wave-mode decomposition: We apply an anisotropic-Helmholtz decomposition method (Zhang et al., 2022), which adapts to arbitrary complex media, and can efficiently produce vector qP- and qS-wavefield with correct amplitudes and phases. 2) Phase angle calculation: The decomposed qP- and qS-wavefields are directionly utilized to calculate the polarization and phase angles. The PP- and PS-images are sorted by the obtained phase angles to produce the ADCIGs. Since we do not require any additional transformation between these two angles in the space domain, there is no additional cost. 3) RMO analysis: We derive a simple expression of group angle from approximated eigenvalues of the VTI Christoffel equation and obtain a concise RMO expression for PP-reflections of flat reflectors. In addition, the AVA analysis (Ruger, 1997; Zhou et al., 2020) is also used to test the amplitude response of our produced ADCIGs.

The paper is organized as follows: We first review the anisotropic- Helmholtz decomposition method for separating P/S wave-mode in VTI media. Then, we bridge polarization angles to phase angles and construct the corresponding ADCIGs in VTI ERTM. Finally, we reframe the RMO formulation based on our derived group-angle expression in VTI media. Two examples for RMO, AVA analysis and ADCIGs are selected to demonstrate the effectiveness and feasibility of our method.

2. Methodology

2.1. Anisotropic-Helmholtz decomposition method

In anisotropic media, the wave propagation is neither parallel nor perpendicular to their polarization direction. The classical Helmholtz decomposition cannot be used to separate the anisotropic wavefields. We present an anisotropic-Helmholtz decomposition method (Zhang et al., 2022) for separating the original wavefields into vector qP- and qS-wavefields in VTI media.

The two dimensional VTI wave equation (Aki and Richards, 2002) is expressed as

$$\begin{aligned}\rho(\mathbf{x})\partial_t^2 u_x(\mathbf{x},t) &= \left[c_{11}(\mathbf{x})\partial_x^2 + c_{55}(\mathbf{x})\partial_z^2\right]u_x(\mathbf{x},t) + [c_{13}(\mathbf{x}) + c_{55}(\mathbf{x})]\partial_{xz}^2 u_z(\mathbf{x},t),\\ \rho(\mathbf{x})\partial_t^2 u_z(\mathbf{x},t) &= [c_{13}(\mathbf{x}) + c_{55}(\mathbf{x})]\partial_{xz}^2 u_x(\mathbf{x},t) + \left[c_{55}(\mathbf{x})\partial_x^2 + c_{33}(\mathbf{x})\partial_z^2\right]u_z(\mathbf{x},t),\end{aligned} \tag{1}$$

where u_x and u_z represent the x- and z-components of the elastic wavefield, respectively. $\mathbf{x} = (x, z)$ is the 2D spatial Cartesian coordinate, t is time, ∂_t^2 is the second-order temporal partial gradient, ∂_x^2 and ∂_z^2 are the second-order partial gradient over x- and z-direction. ∂_{xz} is the mixed spatial partial gradient. ρ is the density. c_{ij} is the stiffness matrix of VTI media, which are shown as

$$\begin{aligned}c_{11} &= (1+2\varepsilon)\rho {v_p}^2, c_{33} = \rho {v_p}^2, c_{55} = \rho {v_s}^2,\\ c_{13} &= \rho\sqrt{[(1+2\delta){v_p}^2 - {v_s}^2][{v_p}^2 - {v_s}^2]} - \rho {v_s}^2,\end{aligned} \tag{2}$$

where v_p and v_s represent the vertical velocity of qP- and qS-waves, respectively. ε and δ are the anisotropic parameters (Thomsen, 1986). We use a plane wave expression as the solution of Eq. (1):

$$u_n = U_n e^{i(k_x x - k_z z - \omega t)},\ n = x,\ z \tag{3}$$

where $U_n\,(n = x, z)$ represents the Fourier transform of u_x and u_z, k_x and k_z are the horizontal and vertical components of the wavenumber. ω represents the angular frequency.

Substituting Eq. 3 into Eq (1) results in the Christoffel equation of VTI meida as:

$$\begin{bmatrix} c_{11}k_x^2 + c_{55}k_z^2 - \lambda & (c_{13}+c_{55})k_x k_z \\ (c_{13}+c_{55})k_x k_z & c_{55}k_x^2 + c_{33}k_z^2 - \lambda \end{bmatrix}\begin{bmatrix} U_x \\ U_z \end{bmatrix} = 0, \tag{4}$$

where the eigenvalue $\lambda = \rho\omega^2 = \rho k^2 V^2$, V represents the P- and S-wave phase velocities, the eigenvector $(U_x, U_z)^T$ indicates the qP- and qS-wave polarization (Dellinger, 1991; Tsvankin, 2012). The approximated solutions of Eq. (4) are shown as (details in Appendix A)

$$\begin{aligned}\lambda_1 &= \rho v_p^2\left[(1+2\varepsilon)k_x^2 + k_z^2\right],\\ \lambda_2 &= \rho v_s^2\left[k_x^2 + k_z^2\right],\end{aligned} \tag{5}$$

and

$$\begin{aligned}\mathbf{D} &= \begin{bmatrix} k_x \\ \dfrac{\sqrt{[(1+2\delta)v_p^2 - v_s^2][v_p^2 - v_s^2]}}{(1+2\varepsilon)v_p^2 - v_s^2}k_z \end{bmatrix},\\ \mathbf{D}^{\perp} &= \begin{bmatrix} \dfrac{\sqrt{[(1+2\delta)v_p^2 - v_s^2][v_p^2 - v_s^2]}}{(1+2\varepsilon)v_p^2 - v_s^2}k_z \\ -k_x \end{bmatrix},\end{aligned} \tag{6}$$

where the eigenvectors $\mathbf{D}$ and $\mathbf{D}^{\perp}$ are the polarization vector of qP- and qS-waves in VTI media, respectively.

Next, an original wavefield $\mathbf{U}$ is defined and separated in the wavenumber domain as

$$\mathbf{U} = \mathbf{U^P} + \mathbf{U^S} \tag{7}$$

where $\mathbf{U} = (U_x, U_z)$ is a vector wavefield. $\mathbf{U^P} = (U_x^p, U_z^p)$ and $\mathbf{U^S} = (U_x^s, U_z^s)$ are the vector P- and S-wavefield, respectively. We project wavefields $\mathbf{U}$, $\mathbf{U^P}$ and $\mathbf{U^S}$ into the qP- and qS-wave polarization $\mathbf{D}$ and $\mathbf{D}^{\perp}$ as

$$\begin{aligned}\mathbf{D}\cdot\mathbf{U} &= \mathbf{D}\cdot\mathbf{U^P},\\ \mathbf{D}^{\perp}\cdot\mathbf{U} &= \mathbf{D}^{\perp}\cdot\mathbf{U^S},\\ \mathbf{D}^{\perp}\cdot\mathbf{U^P} &= 0,\\ \mathbf{D}\cdot\mathbf{U^S} &= 0.\end{aligned} \tag{8}$$

we replace $\mathbf{D}^{\perp}$ with $\mathbf{D}$, and Eq. (8) becomes

$$\begin{aligned}\mathbf{D}\cdot\mathbf{U} &= \mathbf{D}\cdot\mathbf{U^P},\\ \mathbf{D}\times\mathbf{U} &= \mathbf{D}\times\mathbf{U^S},\\ \mathbf{D}\times\mathbf{U^P} &= 0,\\ \mathbf{D}\cdot\mathbf{U^S} &= 0.\end{aligned} \tag{9}$$

where the notation $\cdot$ and $\times$ represent the dot and out product, respectively. Equation (9) contains four unknown variables U_x^p, U_z^p, U_x^s and U_z^s, which are solved as

$$\begin{aligned}U_x^p &= (k_x^2 U_x + r k_z k_x U_z)\big/(k_x^2 + r^2 k_z^2),\\ U_z^p &= (r k_z k_x U_x + r^2 k_z^2 U_z)\big/(k_x^2 + r^2 k_z^2),\\ U_x^s &= (r^2 k_z^2 U_x - r k_z k_x U_z)\big/(k_x^2 + r^2 k_z^2),\\ U_z^s &= (-r k_z k_x U_x + k_x^2 U_z)\big/(k_x^2 + r^2 k_z^2).\end{aligned} \tag{10}$$

with

$$r = \frac{\sqrt{[(1+2\delta)v_p^2 - v_s^2][v_p^2 - v_s^2]}}{(1+2\varepsilon)v_p^2 - v_s^2}. \tag{11}$$

we rewrite Eq. (10) with the vector format as

$$\begin{aligned}\mathbf{U^P} &= \mathbf{D}(\mathbf{D}\cdot\mathbf{U}\big/|\mathbf{D}|^2),\\ \mathbf{U^S} &= -\mathbf{D}\times(\mathbf{D}\times\mathbf{U}\big/|\mathbf{D}|^2).\end{aligned} \tag{12}$$

Equation (12) is the P/S wave-mode decomposed formulations in the wavenumber domain. The polarization vector $\mathbf{D}$ represents the anisotropic-Helmholtz decomposition operator of the wavenumber domain. Moreover, based on weakly anisotropic assumption (Tsvankin, 2012), we conduct the first-order Taylor approximation on the $1/|\mathbf{D}|^2$ of Eq. (12) around $\delta = 0$, $\varepsilon = 0$ and obtain

$$\frac{1}{|\mathbf{D}|^2} = \frac{1}{k_x^2 + r^2 k_z^2} \approx \frac{1}{k_x^2 + k_z^2} + \frac{k_z^2}{(k_x^2 + k_z^2)^2}\cdot\frac{2v_p^2(2\varepsilon - \delta)}{v_p^2 - v_s^2}. \tag{13}$$

we substitute Eq. (13) with Eq. (12) and obtain the space-domain equation as

$$\begin{aligned}\mathbf{u^p} &= \nabla'(\nabla'\cdot\mathbf{w}),\\ \mathbf{u^s} &= -\nabla'\times(\nabla'\times\mathbf{w}),\end{aligned} \tag{14}$$

and

$$\mathbf{w} = -FFT^{-1}\left[\frac{\mathbf{U}}{k_x^2+k_z^2}\right] - FFT^{-1}\left[\frac{k_z^2\mathbf{U}}{(k_x^2+k_z^2)^2}\right]\cdot\frac{2v_p^2(2\varepsilon-\delta)}{v_p^2-v_s^2} \tag{15}$$

where the elastic wavefield $\mathbf{U}$ can be computed by $FFT[\mathbf{u}]$. The operators FFT^{-1} and FFT represent the inverse and forward Fast Fourier transform (FFT), respectively. $\mathbf{u} = (u_x, u_z)$ is the elastic wavefield in the space domain. $\mathbf{u_p} = (u_x^p, u_z^p)$ and $\mathbf{u^s} = (u_x^s, u_z^s)$ represent the decomposed qP- and qS-wavefield in the space domain. ∇' is the anisotropic-Helmholtz decomposition operator of the space-domain and can be written as

$$\nabla' = \begin{bmatrix} \partial_x \\ \dfrac{\sqrt{[(1+2\delta)v_p^2-v_s^2][v_p^2-v_s^2]}}{(1+2\varepsilon)v_p^2-v_s^2}\partial_z \end{bmatrix}. \tag{16}$$

The anisotropic-Helmholtz decomposition method using Eqs. (14) and (15) is performed in the space-wavenumber domain and requires three FFTs. A workflow is summarized in Algorithms 1 and 2 in Zhang et al. (2022).

2.2. Phase angle, polarization angle, and ADCIGs in VTI media

It is known that the angles of phase velocity, polarization, and group velocity are not identical in anisotropic media. In this subsection, we aim to connect the polarization and phase angles to the anisotropic-Helmholtz operator $\mathbf{D}$ that represents qP-wave polarization and is orthogonal to qS-wave polarization.

To start with, we define the phase angle as θ in VTI media and it is easily expressed with the wavenumber as

$$\theta = \arctan\left(\frac{k_x}{k_z}\right), \tag{17}$$

where $k_x = k\sin\theta$, $k_z = k\cos\theta$. The ADCIGs are formulated as the function of θ at the reflectors.

Next, we derive the unit vector of $\mathbf{D}$ as

$$\frac{\mathbf{D}}{|\mathbf{D}|} = \left(\frac{k_x}{\sqrt{k_x^2+r^2k_z^2}}, \frac{rk_z}{\sqrt{k_x^2+r^2k_z^2}}\right) = (\sin\alpha, \cos\alpha), \tag{18}$$

with

$$r = \frac{\sqrt{[(1+2\delta)v_p^2-v_s^2][v_p^2-v_s^2]}}{(1+2\varepsilon)v_p^2-v_s^2}. \tag{19}$$

where α is considered as the polarization angle for qP- and qS-waves in VTI media. Moreover, according to Eqs. (17) and (18), the relationship between α and θ is expressed as

$$\tan\alpha = \frac{k_x}{rk_z} = \frac{1}{r}\tan\theta. \tag{20}$$

by using Eq. (20), the phase angle θ can be obtained from polarization angle α.

To calculate the polarization angle α, we rewrite Eq. (12) as

$$\begin{aligned}\mathbf{U^p} &= \frac{\mathbf{D}}{|\mathbf{D}|}\left(\frac{\mathbf{D}}{|\mathbf{D}|}\cdot\mathbf{U}\right),\\ \mathbf{U^s} &= -\frac{\mathbf{D}}{|\mathbf{D}|}\times\left(\frac{\mathbf{D}}{|\mathbf{D}|}\times\mathbf{U}\right).\end{aligned} \tag{21}$$

by substituting Eq. (18) to Eq. (21), we obtain

$$\begin{aligned}U_x^p &= \sin\alpha(\sin\alpha U_x + \cos\alpha U_z),\\ U_z^p &= \cos\alpha(\sin\alpha U_x + \cos\alpha U_z),\\ U_x^s &= -\cos\alpha(-\cos\alpha U_x + \sin\alpha U_z),\\ U_z^s &= \sin\alpha(-\cos\alpha U_x + \sin\alpha U_z).\end{aligned} \tag{22}$$

we then convert Eq. (22) to the space domain as

$$\begin{aligned}u_x^p &= \sin\alpha(\sin\alpha u_x + \cos\alpha u_z),\\ u_z^p &= \cos\alpha(\sin\alpha u_x + \cos\alpha u_z),\\ u_x^s &= -\cos\alpha(-\cos\alpha u_x + \sin\alpha u_z),\\ u_z^s &= \sin\alpha(-\cos\alpha u_x + \sin\alpha u_z).\end{aligned} \tag{23}$$

According to Eq. (23), we can calculate the polarization angle in the space domain via:

$$\tan\alpha = \frac{u_x^p}{u_z^p}, \tag{24}$$

or

$$\tan\alpha = -\frac{u_z^s}{u_x^s}. \tag{25}$$

By substituting Eq. (24) or Eq. (25) to Eq. (20), we obtain the expression of phase angle as

$$\tan\theta = r\frac{u_x^p}{u_z^p}, \tag{26}$$

or

$$\tan\theta = -r\frac{u_z^s}{u_x^s}. \tag{27}$$

Equations (24) and (25) show the polarization angle α of qP- and qS-waves, while Eqs. (26) and (27) represent the phase angle θ of qP- and qS-waves, respectively.

In this paper, we mainly focus on the PP- and PS-images. Therefore, we use the separated vector qP-wavefield (the source side) to calculate the phase angle as incident angle aperture (assume the reflectors are flat or nearly flat so that the dips are almost zero) for extracting ADCIGs in VTI ERTM. The specific expression is written as:

$$\begin{aligned}I^{pp}(\mathbf{x},\theta_1) &= \int_0^T \mathbf{S^p}(\mathbf{x},t)\cdot\mathbf{R^p}(\mathbf{x},t)\cdot\delta'(\theta-\theta_1)\mathrm{d}t,\\ I^{ps}(\mathbf{x},\theta_1) &= \int_0^T \mathbf{S^p}(\mathbf{x},t)\cdot\mathbf{R^s}(\mathbf{x},t)\cdot\delta'(\theta-\theta_1)\mathrm{d}t.\end{aligned} \tag{28}$$

here, $I^{pp}(\mathbf{x},\theta_1)$ and $I^{ps}(\mathbf{x},\theta_1)$ are the PP- and PS-ADCIGs, respectively. $\mathbf{S^p}(\mathbf{x}, t)$ represents the separated qP-wavefield in source side. $\mathbf{R^p}(\mathbf{x}, t)$ and $\mathbf{R^s}(\mathbf{x}, t)$ represent the separated qP- and qS-wavefield from the receiver side. $\delta'(\theta - \theta_1)$ equals 1 only with $\theta = \theta_1$ otherwise it

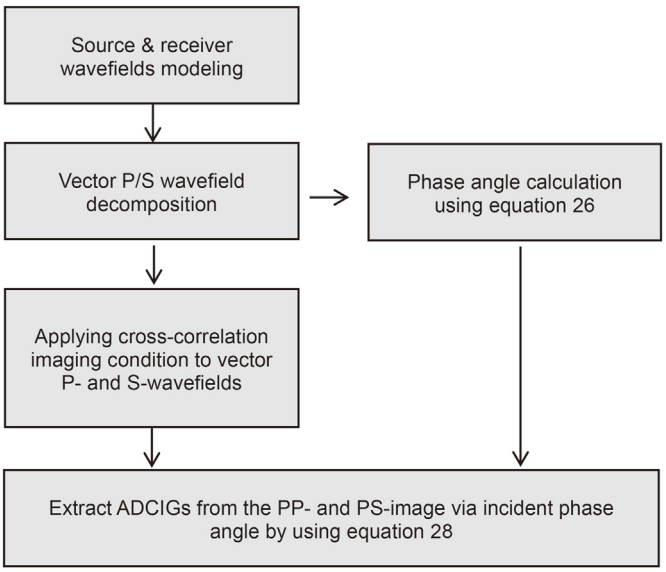

Fig. 1. The workflow for extracting ADCIGs in VTI ERTM by using the proposed method.

equals 0. θ is the calculated phase angle and θ_1 is the chosen angle for ADCIGS extraction. The incident phase angles are obtained from the qP-wavefield of the source side. T is the maximum propagation time. A flowchart is shown in Fig. 1 for understanding our proposed extracting ADCIGs method.

Meantime, the description of workflow for extracting ADCIGs in VTI ERTM can be expressed as follows.

(1) Solving the VTI wave equation and obtaining the source wavefields $\mathbf{S}(\mathbf{x}, t)$.
(2) Using the anisotropic-Helmholtz decomposition method to acquire decomposed $\mathbf{S}^{\mathbf{p}}(\mathbf{x}, t)$ and $\mathbf{S}^{\mathbf{s}}(\mathbf{x}, t)$ wavefields.
(3) Solving the adjoint VTI wave equation and obtaining the receiver wavefield $\mathbf{R}(\mathbf{x}, t)$ with multi-component seismic records.
(4) Using the anisotropic-Helmholtz decomposition method to acquire decomposed $\mathbf{R}^{\mathbf{p}}(\mathbf{x}, t)$ and $\mathbf{R}^{\mathbf{s}}(\mathbf{x}, t)$ wavefields.
(5) Calculating the phase angle of qP-wavefield on the source side by using Eq. (26) at each point in the space domain for every snapshot.
(6) Using the dot-product cross-correlation imaging condition (Eq. (28)) to generate ADCIGs.

2.3. Residual moveout and group angle in VTI media

The ADCIGs reveal flat events for correct velocities. Any moveouts in the ADCIGs can be used to improve the migration velocity model. Biondi (2007b) presents the RMO Δ_{RMO} in anisotropic PP-ADCIGs for reflections of flat reflectors as

$$\Delta_{\mathrm{RMO}} = \rho_v Z_0 \tan\theta \tan\psi, \tag{29}$$

where ρ_v is the velocity perturbation ratio, Z_0 is the depth of events, θ is the incident phase angle, and ψ is the group angle representing the propagation of group velocity. The difficulty of implementing Eq. (29) increases due to the complex transformation from the phase angle to the group angle.

The general expression of group velocity $\mathbf{V}_G$ is shown as (Berryman, 1979; Tsvankin, 2012)

$$\mathbf{V}_G = \nabla(kV) = \frac{\partial(kV)}{\partial k_x}\vec{\mathbf{x}} + \frac{\partial(kV)}{\partial k_z}\vec{\mathbf{z}}, \tag{30}$$

where ∇ is the spatial gradient operator, k_x and k_z are wavenumber components in x- and z-direction. $\vec{\mathbf{x}}$ and $\vec{\mathbf{z}}$ are base vectors in the x- and z-axis. kV can be obtained from the eigenvalue of the Christoffel equation (Eq. (4)). In terms of Eq. (30), the tangent of the group angle in Eq. (29) can be expressed as

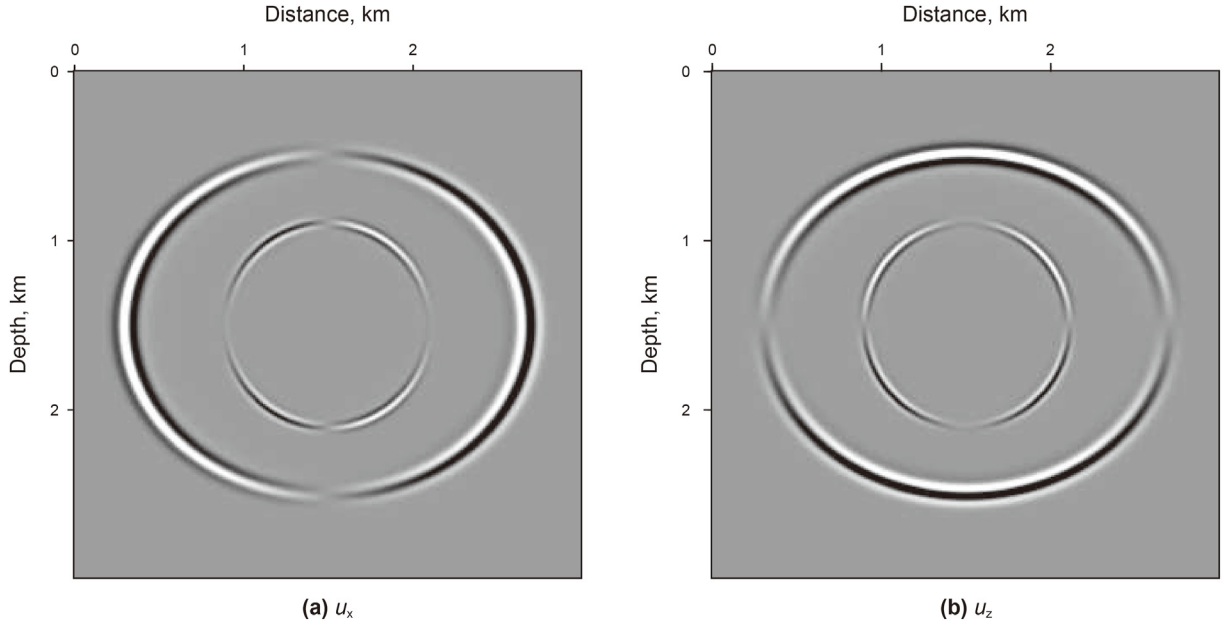

Fig. 2. Original elastic wavefield components of VTI homogeneous model in (a) x- and (b) z-direction with propagation time 0.5 s.

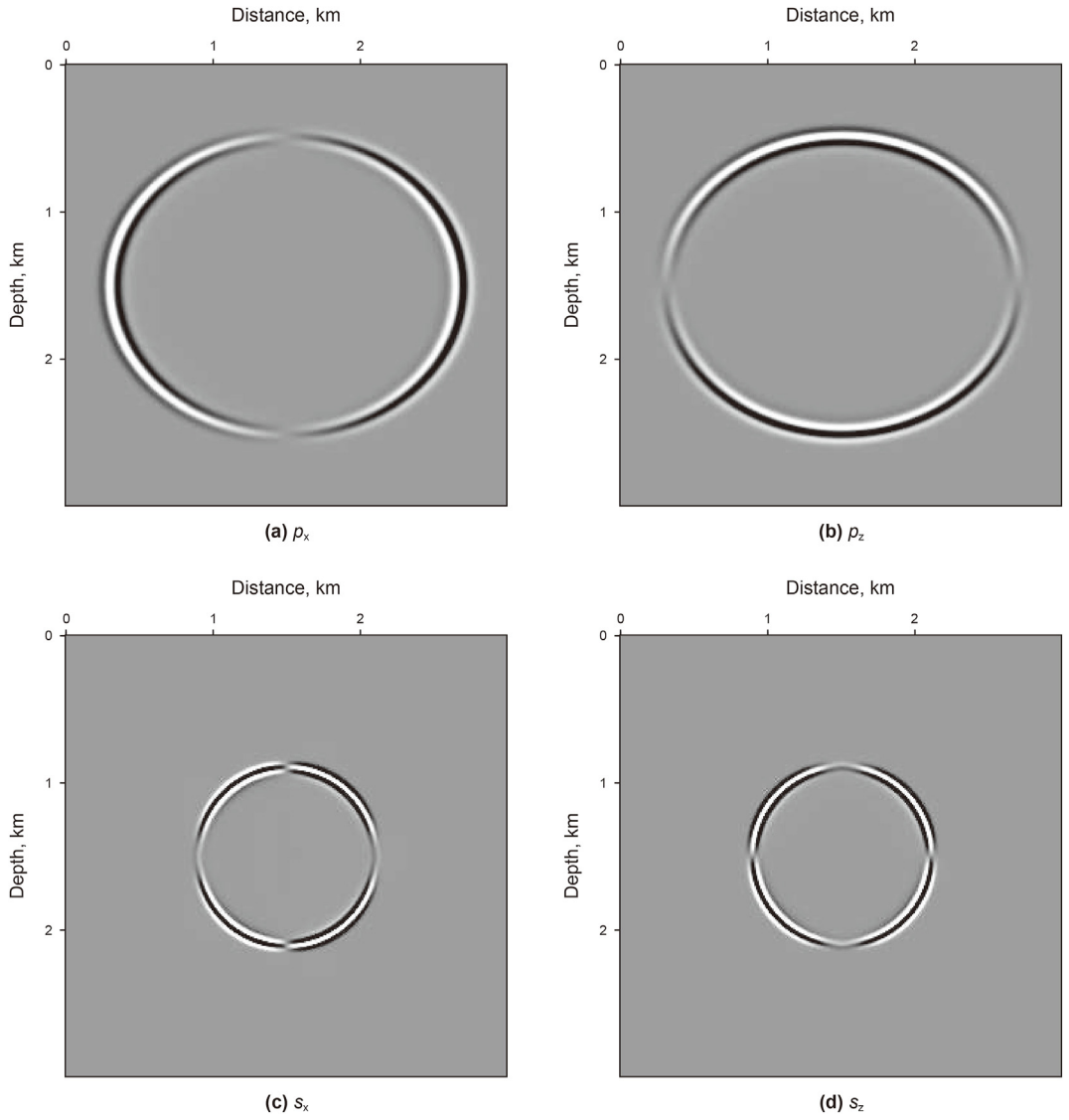

Fig. 3. Separated P-wavefields and S-wavefields of VTI homogeneous model via the anisotropic-Helmholtz decomposition approach. Panels (a) and (b) are *x*- and *z*-components of vector P-wavefield, (c) and (d) are vector S-wavefield components in *x*- and *z*-direction.

$$\tan\psi = \frac{\partial(kV)}{\partial k_x} \Big/ \frac{\partial(kV)}{\partial k_z}. \tag{31}$$

Equation (31) represents the group angle of qP- or qS-wave. Because we mainly analyze the RMO of PP-ADCIGs, the group angle of P-wave is focused. The analytical expression of the qP-wave group angle can be calculated from the exact eigenvalue of the Christoffel equation (Eq. (A7)). We substitute the analytical group-angle expression into Eq. (29) and obtain a complex formulation of the RMO curve (Biondi RMO curve). To simplify it, we conduct a succinct expression of qP-wave group velocity using the approximated eigenvalue (first item of Eq. (5)):

$$\mathbf{V}_{G_P} = \frac{(1+2\varepsilon)v_p k_x}{\sqrt{(1+2\varepsilon)k_x^2 + k_z^2}}\vec{\mathbf{x}} + \frac{v_p k_z}{\sqrt{(1+2\varepsilon)k_x^2 + k_z^2}}\vec{\mathbf{z}}. \tag{32}$$

we then substitute Eq. (32) into Eq. (31) and obtain the approximated group-angle expression of qP-wave as

$$\tan\psi_P = \frac{(1+2\varepsilon)k_x}{k_z} = (1+2\varepsilon)\tan\theta. \tag{33}$$

Furthermore, by substituting Eq. (33) into Eq. (29) we can obtain the approximated RMO of PP-ADCIGs as

$$\Delta_{\mathrm{RMO}_{PP}} = \rho_v Z_0 (1+2\varepsilon)\tan^2\theta. \tag{34}$$

Equation (34) relieves the complexity of the group-angle computation of Eq. (29). In the numerical tests, we compare our proposed RMO curve with the classical Biondi's RMO curve via our produced ADCIGs.

3. Examples

In this section, a simple and a complicated model (the Hess model) are used to demonstrate the effectiveness of our proposed methods. Moreover, we used first-order elastic wave equation (Qu et al., 2022) and eight-order staggered-grid finite difference to extrapolate wavefields and apply perfect matching layer boundary

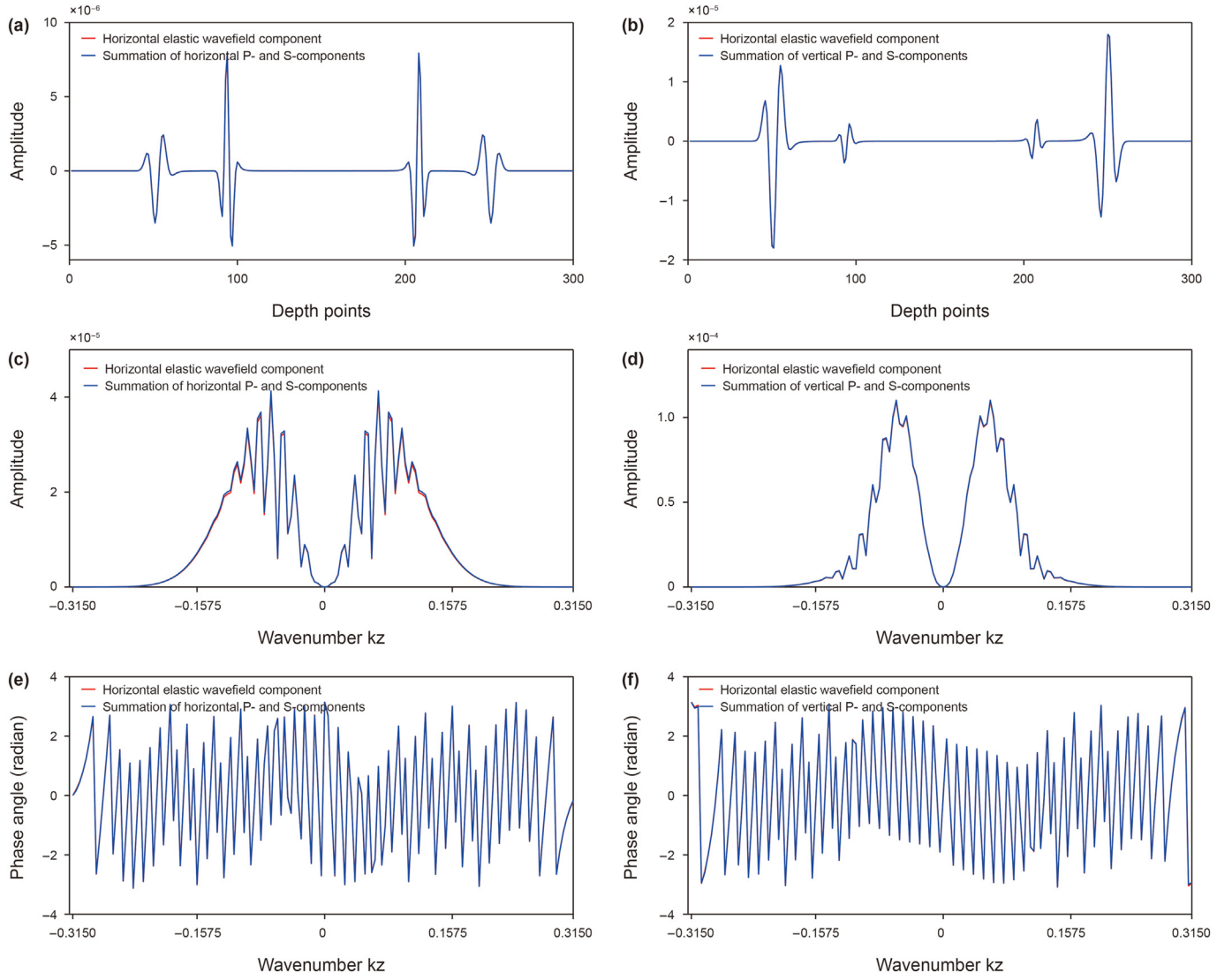

Fig. 4. Comparison of trace data extracted from original elastic wavefield (Fig. 2) and separated P/S wavefields (Fig. 3) at distance of 1600 m. Panel (a) represents horizontal (x-) elastic and summation of P- and S-wavefields components and (b) is vertical (z-) elastic and summation of P- and S-wavefield components. (c) and (d) are the amplitude spectrum of half depth points (from 0 to 150) in (a) and (b), respectively, (e) and (f) are the phase spectrum of half depth points (from 0 to 150) in (a) and (b), respectively. The red lines represent original elastic wavefield components and blue lines are the summation of P- and S-wavefield components.

condition to absorb artificial reflections.

3.1. VTI homogeneous model

To start with, we use a simple VTI homogeneous model to demonstrate that the anisotropic-Helmholtz decomposition method can produce the P- and S-wavefields with correct amplitudes and phases as the original wavefields. The elastic parameters are $v_p = 2500$ m/s, $v_s = 1500$ m/s, $\rho = 1.0$ g/cm^3 and the anisotropic parameters are $\varepsilon = \delta = 0.2$. The model is discreted by grid size of 300×300 with a spacing of 10 m. The 15 Hz Ricker wavelet is set as center of model with a temporal interval of 1 ms. As observed, Fig. 2 represents the original elastic wavefields at propagating time of 0.5 s. By using the anisotropic-Helmholtz decomposition method, Fig. 3 exhibits the separated P- and S-wavefield components. These wave components show a clear decomposing effect compared with original wave components (Fig. 2). Furthermore, we extract the trace data at distance of 1600 m from Figs. 2 and 3. Fig. 4(a) and (b) compare the original elastic wave components (red lines) with the summation of P- and S-wavefield components (blue lines), which present the corresponding amplitudes and phases. These data are then converted to wavenumber-domain (k_z-domain) to show the amplitude spectrum (Fig. 4(c) and (d)) and phase spectrum (Fig. 4(e) and (f)). As expected, these spectrums (indicated by red lines and blue lines) are consistent with each other, which demonstrate the correct amplitude and phases of the decomposed P- and S-wavefields.

3.2. RMO analysis

It is well-known that the RMO curves are useful tools for MVA. In this subsection, we compare Biondi's RMO with the proposed approximate RMO curves via PP-ADCIGs for different velocity perturbations. In addition, the AVA analysis is also applied to the migrated ADCIGs with correct velocities. A velocity model of Mesa clay shale (Thomsen, 1986; Biondi, 2007b) is selected to analyze the RMO and AVA performance. The corresponding anisotropic parameters are $v_p = 3794$ m/s, $v_s = 2074$ m/s, $\rho = 2.56$ g/cm^3, $\varepsilon = 0.189$

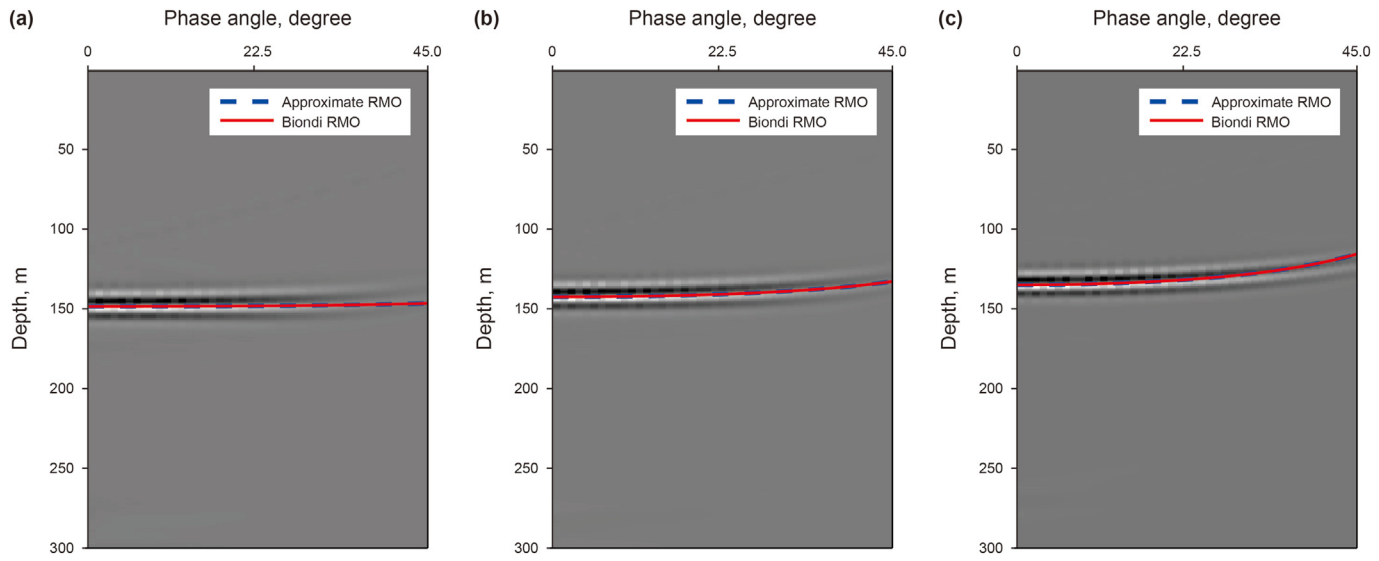

Fig. 5. The PP-ADCIGs and RMO curves with the different negative velocity perturbations. The calculated phase angle range is from 0° to 45°. The ADCIGs are curved up with the (a) 1% lower velocity, (b) 5% lower velocity and (c) 10% lower velocity. The blue dashed lines are the approximate RMO curves and the red solid lines are the Biondi's RMO curves.

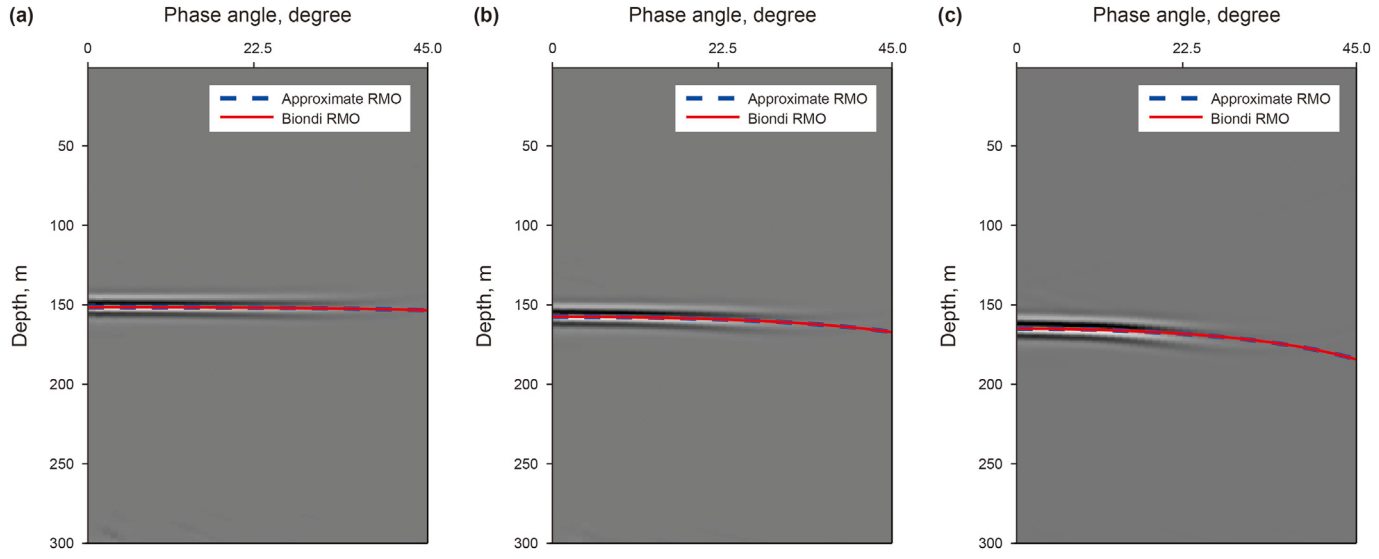

Fig. 6. The PP-ADCIGs and RMO curves with the different positive velocity perturbations. The calculated phase angle range is from 0° to 45°. The ADCIGs are curved up with the (a) 1% higher velocity, (b) 5% higher velocity and (c) 10% higher velocity. The blue dashed lines are the approximate RMO curves and the red solid lines are the Biondi's RMO curves.

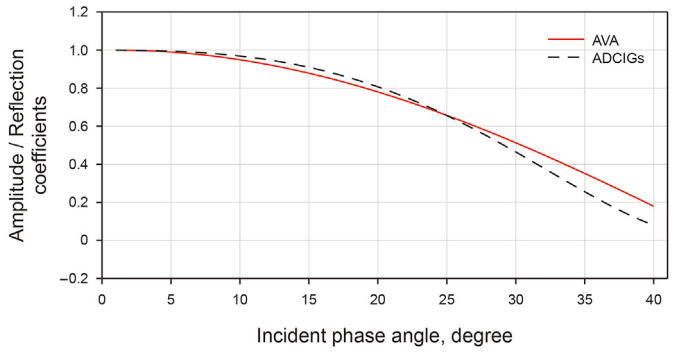

Fig. 7. The PP-ADCIGs and AVA PP-coefficient curves with the given correct velocity models. The calculated phase angle range is from 0° to 40°. The black dashed lines are the PP-ADCIGs and the red solid lines are the AVA curves.

and $\delta = 0.204$. The homogeneous models are discretized with a grid size of 600 × 300 and a spacing interval of 10 m. The explosive source applies a 15 Hz Ricker wavelet with 0.5 ms time interval. A density anomaly $\rho = 2.80$ g/cm^3 is placed at the depth of 1500 m to generate reflections. 600 shots are evenly distributed at the depth of 10 m. For each shot, 600 receivers are distributed on the surface with a spacing of 10 m.

The vertical velocity perturbations ρ_v of qP- and qS-waves are set as ±1%, ±5%, and ±10%. The phase angle range is from 0° to 45°. Figs. 5 and 6 are the migrated PP-ADCIGs overlayed by Biondi's and approximate RMO curves with different positive and negative velocity perturbations. As observed, the curvatures raise as the velocity perturbation and phase angle increase. The depth shifts of interface also become large with the low/high growth of velocities. Moreover, Fig. 5 shows an upgoing curve with the negative velocity perturbations, whereas Fig. 6 exhibits a downgoing curve with the positive velocity perturbations. The approximate RMO curves

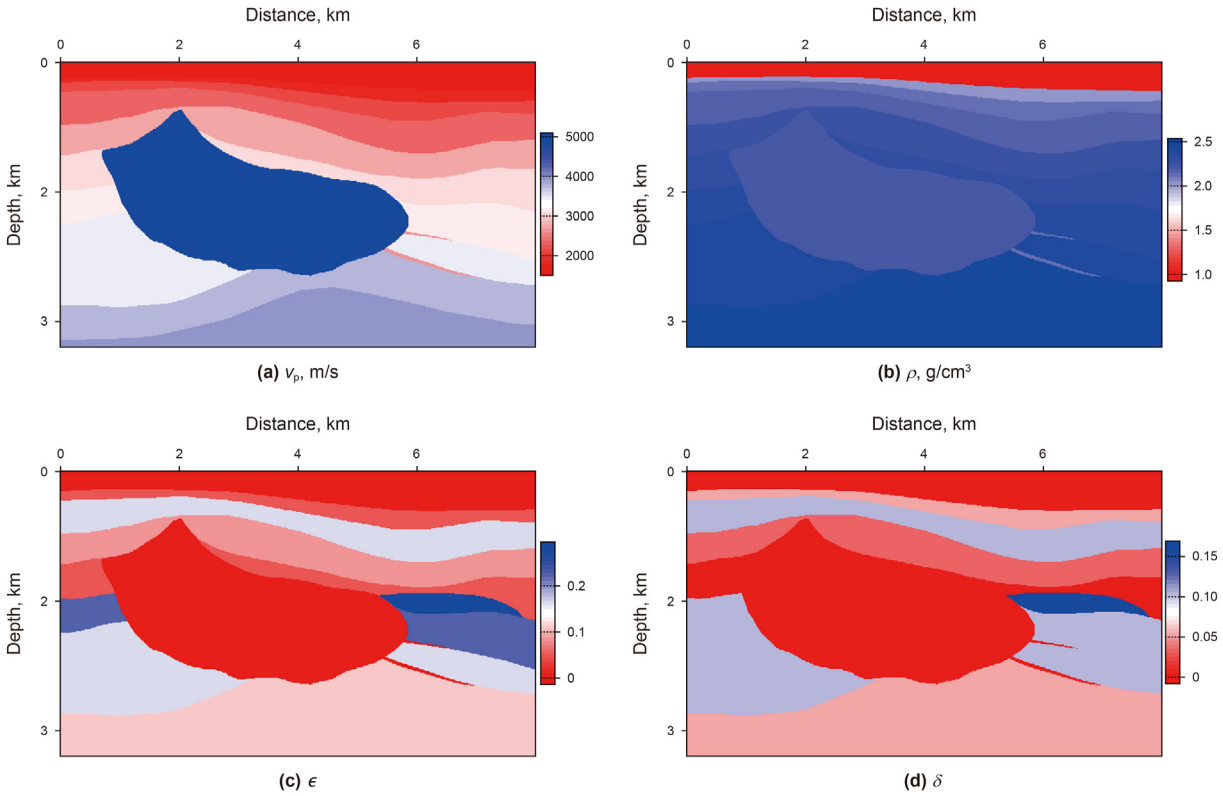

Fig. 8. The VTI Hess model with elastic parameters (a) P-wave velocity, (b) density, and anisotropic parameters (c) ε and (d) δ.

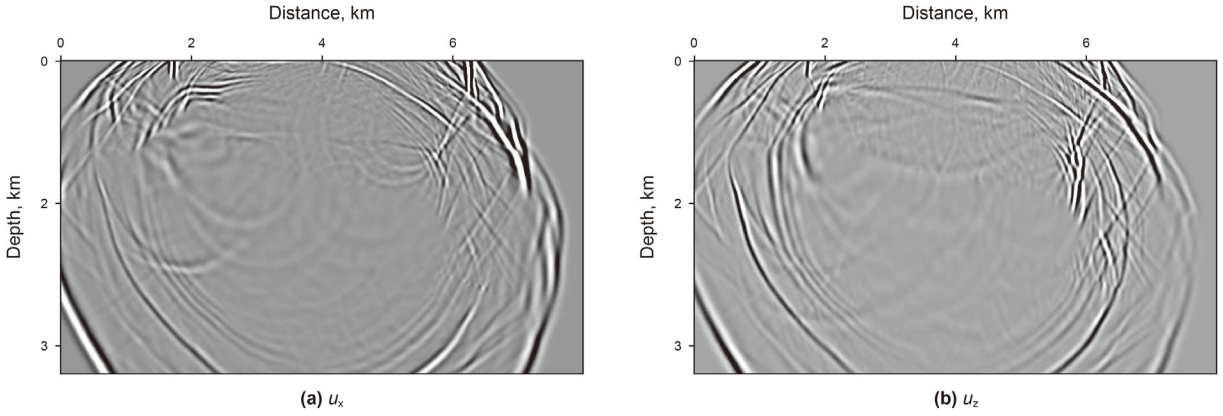

Fig. 9. Elastic wavefield components of Hess model in (a) x- and (b) z-direction with propagation time 1.4 s.

present a good agreement with the Biondi's RMO curves. The gathers show the equivalent up/down moveouts within 45° in comparison to these RMO predictions. These results demonstrate our method can provide a high-quality residual moveout for MVA analysis. In addition, we analyze the AVA response for our ADCIGs with the given correct migrated velocity models. As shown in Fig. 7, the PP-reflection coefficients decrease with the larger incident phase angle. The migrated gathers (black dash line) produce the similar amplitude response as the AVA PP-coefficient curve (red solid line) within 40°. A little difference between two lines is presented at the large incident angle, which is caused by the elliptical and weak anisotropic assumption in our methods.

3.3. VTI Hess model

The VTI Hess model (Fig. 8) is selected to produce PP- and PS-ADCIGs via our proposed method. For simplicity, the S-wave velocity is calculated by dividing the P-wave velocity by 2.0. The

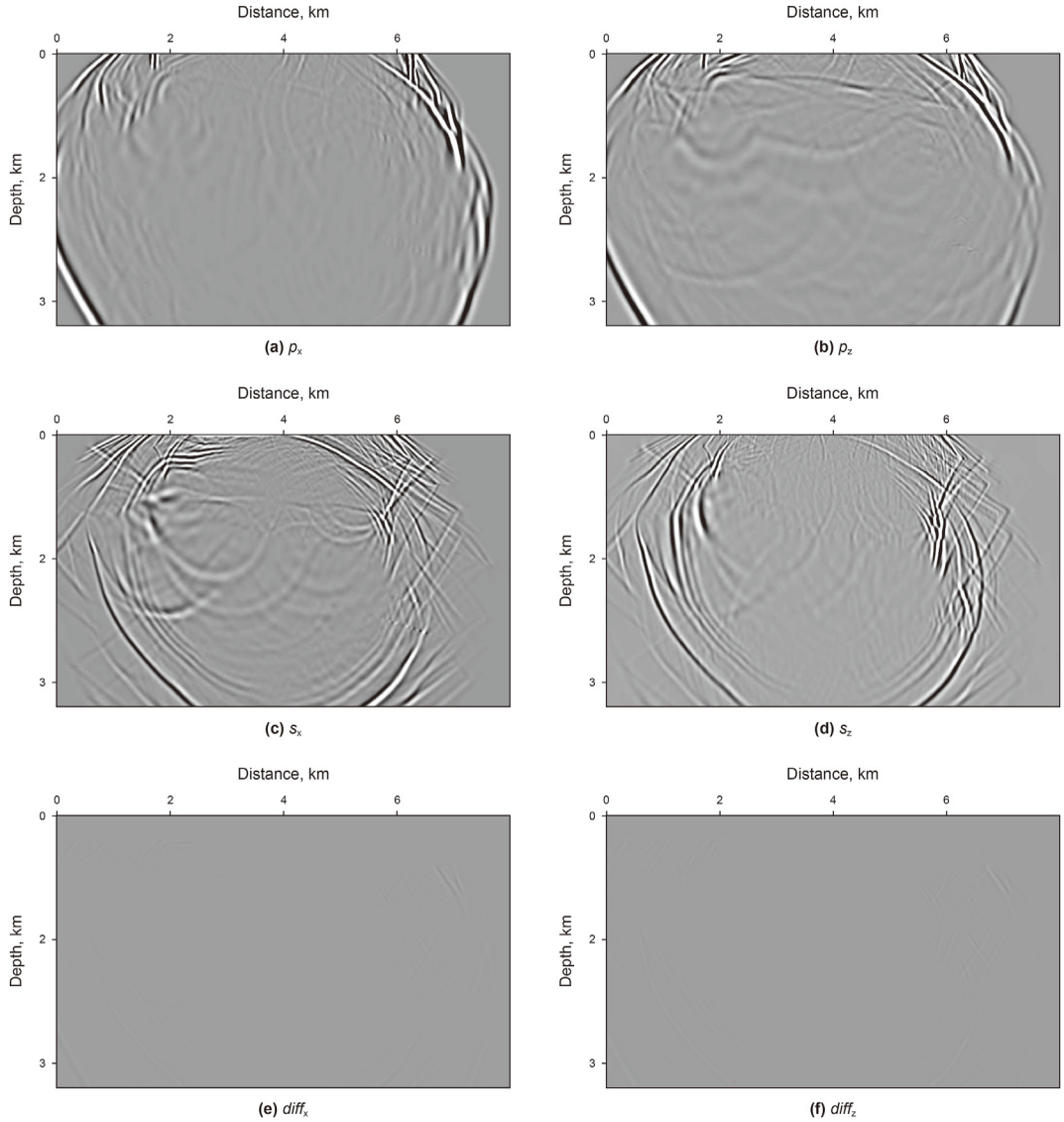

Fig. 10. Separated P-wavefields and S-wavefields of VTI Hess model via the anisotropic-Helmholtz decomposition approach. Panels (a) and (b) are vector P-wavefield components projected on x- and z-direction, (c) and (d) are vector S-wavefield components in x- and z-direction, (e) and (f) are difference calculated from $(p_x + s_x - u_x)$ and $(p_z + s_z - u_z)$, respectively. u_x and u_z are original wavefields shown in Fig. 9.

model is discrete by the grid size of 800 × 330 with a spatial interval of 10 m. A 15 Hz Ricker wavelet is chosen as the source with a time interval of 1 ms. A Gaussian function with the grid size of 10 × 10 is adopted for smoothing true models. 120 shots are evenly excited on the ground with a spatial step of 10 m. 600 receivers are employed to detect multiple-component signals with a split-spread aperture of 6 km.

To start with, we perform a P/S wavefield separation and phase angle calculation experiment. A single source is placed at (4000, 10) m. Fig. 9 is the original vector elastic wavefields at propagating time of 1.4 s. Applying the anisotropic-Helmholtz decomposition method (Eqs. (14) and (15)), Fig. 10(a) and (b) represent the x- and z-components of vector P-wavefields and Fig. 10(c) and (d) show the x- and z-components of vector S-wavefields. The error plots are shown in Fig. 10(e) and (f) demonstrate those wavefields are well separated and can be used to calculate the polarization angles (Eqs. (24) and (25)) and the phase angles (Eqs. (26) and (27)). The polarization angle is defined between the polarization direction and z-axis, while the phase angle is defined between the phase velocity direction and z-axis. The angle range is from $(-\pi/2, \pi/2)$. Fig. 11(a) and (b) show the qP- and qS-wave polarization angles (Eqs. (24) and (25)), respectively. Fig. 11(c) and (d) exhibit the qP- and qS-wave phase angles (Eqs. (26) and (27)), respectively. For each shot, the phase angles are calculated at each time step and used in Eq. (28) (with the horizontal layer assumption) to produce ADCIGs of the Hess model.

Figs. 12 and 13 illustrate the ADCIGs of the Hess model with the different migrated velocities. The ADCIGs exhibit the flat events

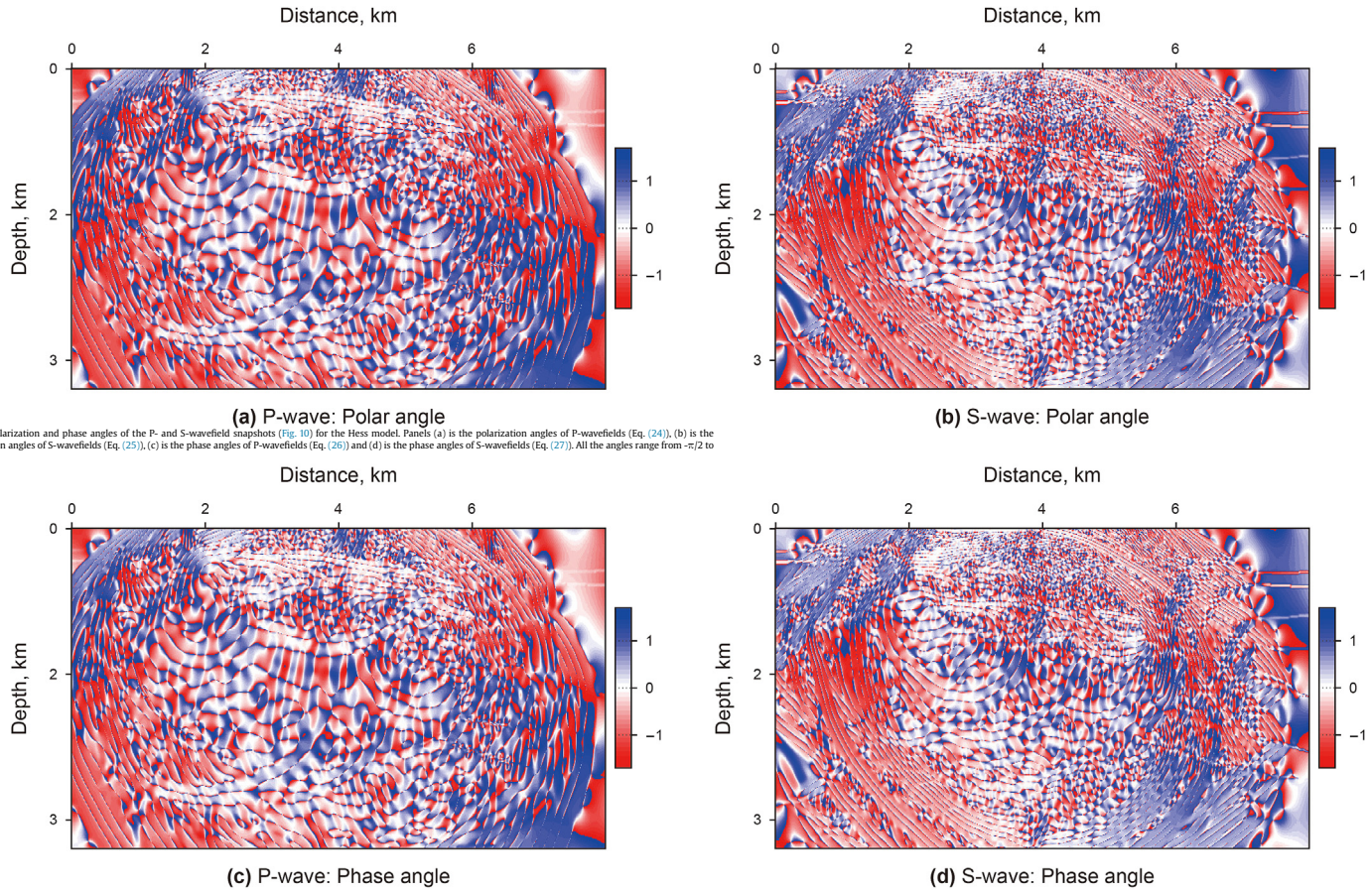

Fig. 11. Polarization and phase angles of the P- and S-wavefield snapshots (Fig. 10) for the Hess model. Panels (a) is the polarization angles of P-wavefields (Eq. (24)), (b) is the polarization angles of S-wavefields (Eq. (25)), (c) is the phase angles of P-wavefields (Eq. (26)) and (d) is the phase angles of S-wavefields (Eq. (27)). All the angles range from -π/2 to π/2.

(Figs. 9(b) and Fig. 10(b)) with the correct velocities, whereas the ADCIGs show upward curves (Figs. 12(a) and Fig. 13(a)) with 5% lower velocities, and exhibit downward curves (Figs. 12(c) and Fig. 13(c)) with 5% higher velocities. The curvatures increase with the growth of phase angle and velocity perturbations. In addition, the phase angle aperture of PS-ADCIGs (Fig. 13) is wider than that of PP-ADCIGs (Fig. 12) due to the larger incident qP-wave angle required by reflected qS-waves. Note that some events at the depth of 1.5 km~3 km (indicated by the arrows in Figs. 12 and 13) do not follow the correct curved tendency caused by multiples and converted waves. The ADCIGs for the correct velocity models (Figs. 12(b) and Fig. 13(b)) are used to produce stack PP- and PS-images (Fig. 14(a) and (b)). For comparison, the anisotropic ERTM method is also used to produce the corresponding images (Fig. 14(c) and (d)), which demonstrates the robustness of our method.

4. Discussion

First, this paper applies the anisotropic-Helmholtz decomposition method for ERTM imaging in VTI media. The separated qP- and qS-wavefields are then used to calculate the polarization- and phase angles. The phase angles are applied to ERTM for ADCIGs extraction. Our method can be easily extended to 3D and TTI media. However, the computational cost will increase at the meantime. Because the local homogeneous assumption is used for deriving the Christoffel equation, a smoothing velocity model is preferred for ERTM implementation. In addition, the weakly anisotropic and elliptical VTI assumptions are used to derive the anisotropic-Helmholtz decomposition operator and three-angle (phase, polarization, group) relations. Therefore, our method may encounter non-negligible errors in the presence of strong non-elliptical media. The accuracy tests regarding these assumptions can be found in Zhang et al. (2022).

Second, we analyze the RMO curves and AVA analysis for the reflections of flat reflectors and extend this study to ADCIGs extraction with steep reflectors (Zhao et al., 2021) that are currently under development. Meantime, we also apply horizontal layer assumption for ADCIGs extraction in Eq. (28). This may influence the angle-axis of Figs. 8–9. Thus, we choose the slight incline events in Hess model such as x=4.25 km to produce ADCIGs images. For Fig. 10, because we stack the PP- and PS-ADCIGs data with a wide phase angle range (−50 to 50), the influence from the horizontal layer assumption can be acceptable and thus we can obtain the identical images (Fig. 14(a) and (b)) as those of anisotropic ERTM (Fig. 14(c) and (d)). Adding the dip angle to Eq. (28) is what we focus on next. In addition, we only discuss the VTI RMO and AVA

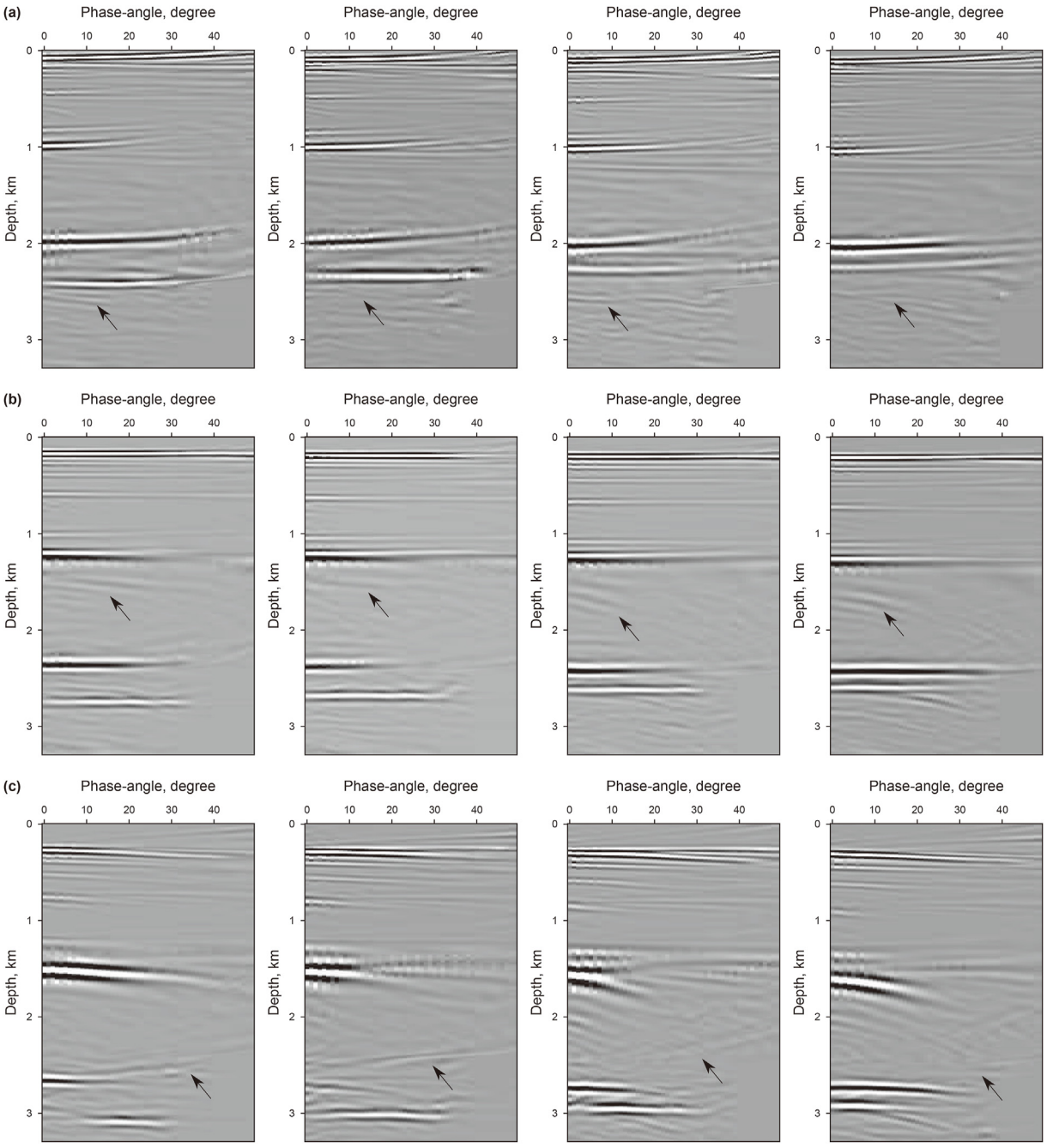

Fig. 12. The PP-ADCIGs of the Hess model at position x=3.50, 3.75, 4.00 and 4.25 km. The calculated phase angle range is from 0° to 50°. The ADCIGs of PP-image are (a) curved up with the 5% lower velocity, (b) flat with the correct velocity and (c) curved down with 5% higher velocity. The black arrows indicate the events imaged by multiples and converted waves.

of PP-ADCIGs, whereas the PS-ADCIGs have not been completely developed due to its complexity in anisotropic media. It is necessary to study this aspect in future research.

Third, we improve the P/S wave-mode decomposition and the phase-angle calculation for anisotropic ADCIGs extraction of ERTM in this paper. To exhibit the advantages, we compare the previous studies and our method in model assumption, computation and angle accuracy. As shown in Table 1, although Poynting vector shows the minimal computation cost, it is usually influenced by the complex wavefield-interference and produces inaccurate angles. The vector P/S wavefield decomposition using local FTs or using low rank approximation requires multiple FTs and cost much computation. Our method integrates the features of these methods regarding high efficiency, angle accuracy and great model adaptability.

Equations (2, 24–27) are used to calculate polarization and phase angles. There may exist many zero values in separated qP-

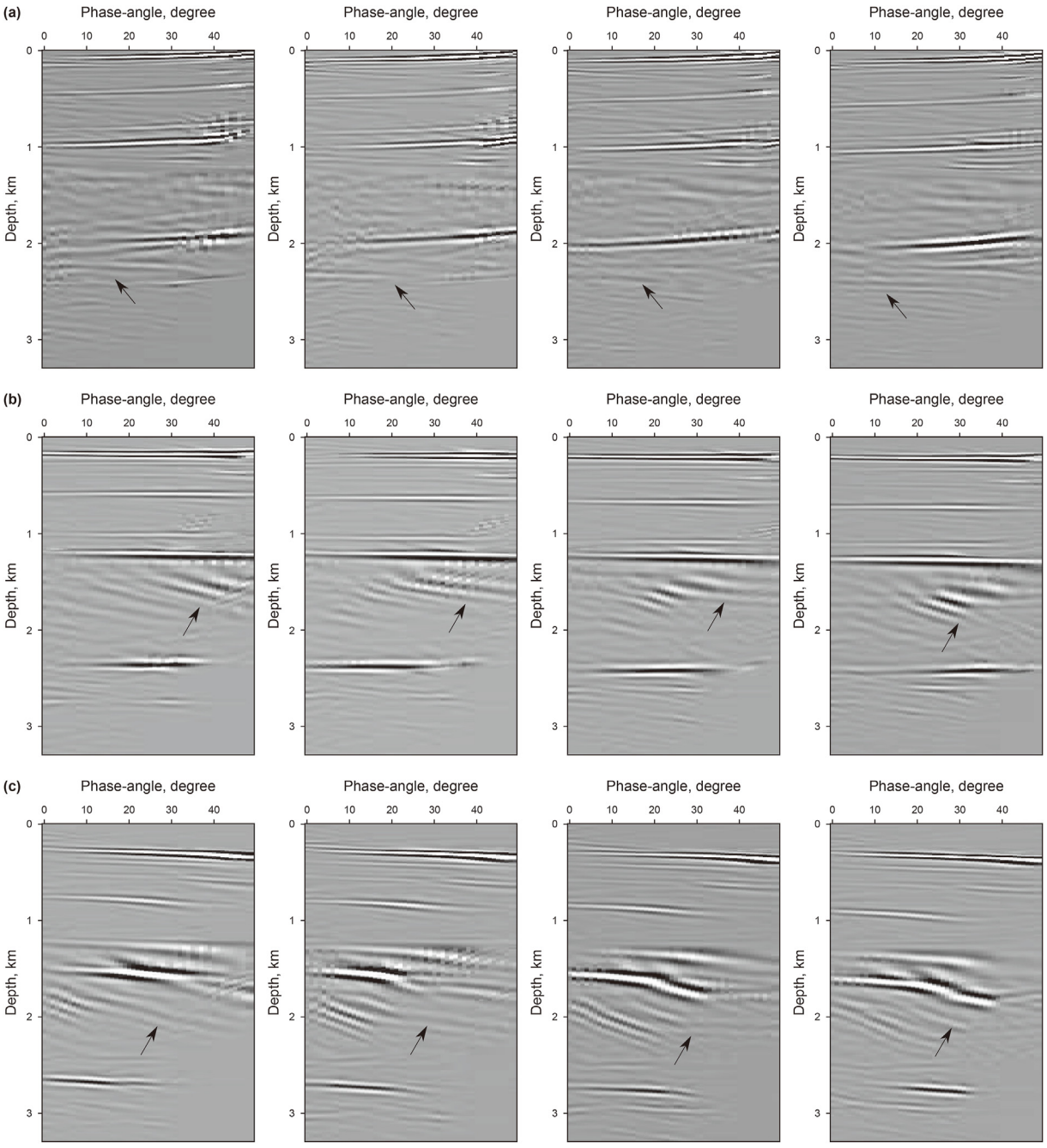

Fig. 13. The PS-ADCIGs of the Hess model at position x=3.50, 3.75, 4.00 and 4.25 km. The calculated phase angle range is from 0° to 50°. The ADCIGs of PS-image are (a) curved up with the 5% lower velocity, (b) flat with the correct velocity and (c) curved down with 5% higher velocity. The black arrows indicate the events imaged by multiples and converted waves.

and qS-wavefields where the waves do not arrive or are influenced by waveform shape. To solve this problem, we add a pretty small positive value in the denominator of Eqs. (2, 24-27). Theses may introduce slight numerical errors for angle calculation. However, the near-zero values contribute little for ADCIGs and images in anisotropic ERTM.

To further improve the computation cost, we apply the GPU technology to all aspects of the ADCIGs extraction including modeling, imaging and angles calculation. In addition, the anisotropic-Helmholtz decomposition method needs three times FFTs at each time step. An optimized FFT function *cufft* from the GPU toolkit is applied to the decomposition process. This makes our method achieve high efficiency in production. However, when the large 3D data are used in our method, the single GPU cannot undertake huge memory. The multi-GPUs strategy may be considered in our research.

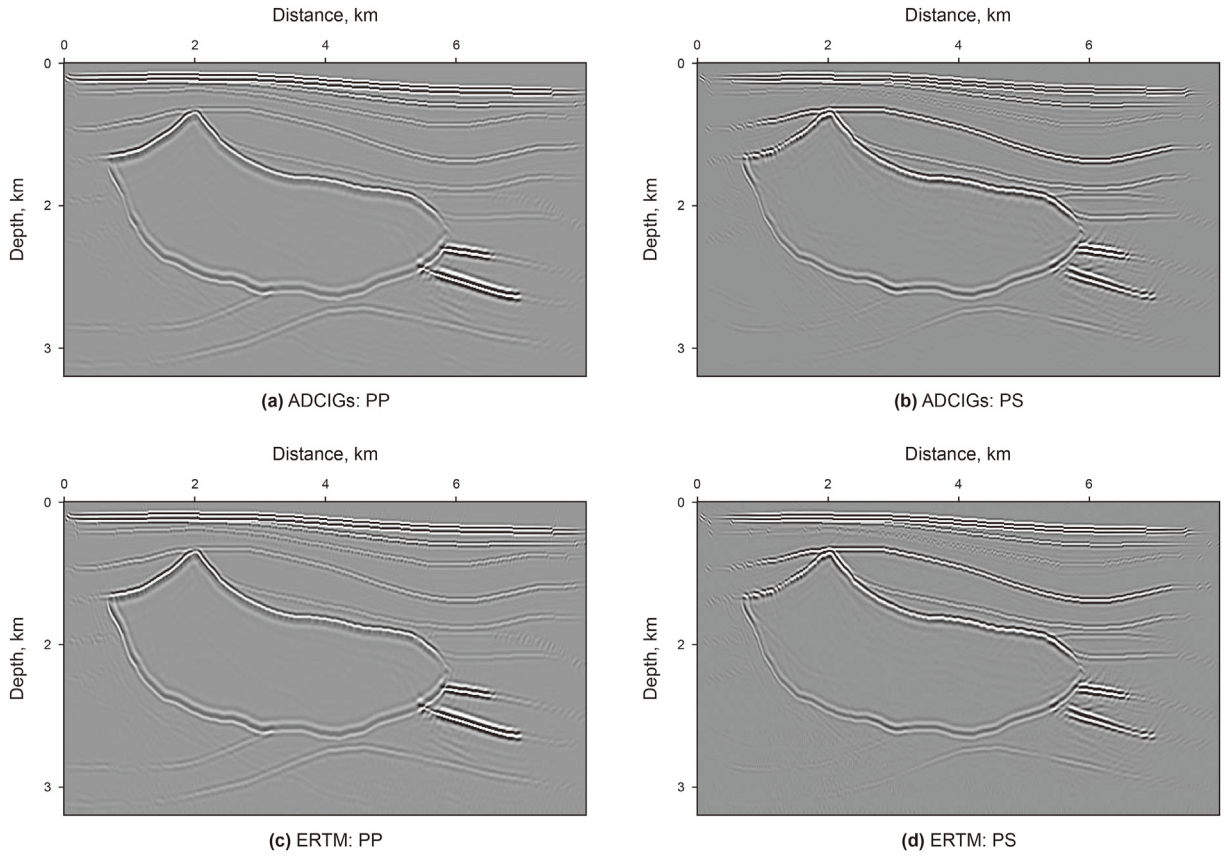

Fig. 14. The produced image results of Hess model using different approaches. Panels (a) PP-image and (b) PS-image use the stacked ADCIGs data (Figs. 12(b) and 13(b)), (c) PP-image and (d) PS-image apply the anisotropic ERTM method. The results exhibit similar imaging effects.

Table 1
Comparison between the previous ADCIGs studies and our method. The angle mentioned in table is for ADCIGs extraction. The computation mainly refer to the cost of P/S decomposition. M represents the number of homogeneous parts. X is rank number for low-rank approximation. N is total grid points of the model.

Method	Angle used	P/S wave-mode decomposition	Model assumption	Computation ∝	Angle accuracy
Poynting vector (Wang and Zhang, 2022)	phase	poynting vector	smoothed	N	low
CIGs in ERTM (Zhang and Mcmechan, 2011a)	polarization	vector P/S decomposition	local homogeneous	$M*N\log_2 N$	high
Scalar and vector imaging (Wang et al., 2016a)	phase	low-rank approximation	smoothed	$X*N\log_2 N$	high
Anisotropic-Helmholtz (this paper)	phase	anisotropic-Helmholtz	smoothed	$3N\log_2 N$	high

5. Conclusion

We apply the anisotropic-Helmholtz decomposition method to ADCIGs extraction in VTI media. This approach adapts to arbitrary heterogeneous media and efficiently separates the original wavefields into vector qP- and qS-wavefields. We then use the separated qP- and qS-wavefields to calculate the polarization and phase angles in the space domain. The phase angle is applied to ERTM imaging for ADCIGs extraction. Compared with the previous studies, our approach shows the advantages in the computation, model adaptability and angle accuracy. In addition, we present a concise approximate RMO expression of PP-ADCIGs for reflections of flat reflectors. The VTI Hess model and Mesa clay shale data examples are seleted to validate the RMO and AVA analysis for produced ADCIGs.

Data availability

The data underlying this paper are available in the paper.

Acknowledgements

We appreciate the help of the Editor and the anonymous reviewers for their comments and suggestions. These significantly improve the quality of this paper. This study is jointly supported by the National Key R&D Program of China (2020YFA0710604 and 2017YFC1500303), the Science Foundation of the China University of Petroleum, Beijing (2462019YJRC007 and 2462020YXZZ047), and the Strategic Cooperation Technology Projects of CNPC and CUPB (ZLZX2020-05).

APPENDIX A

Deriving The Eigenvalues And Eigenvectors From The Christoffel Equation

To start with, we show the Christoffel equation in VTI media (Eq. (4)) as

$$\begin{bmatrix} c_{11}k_x^2 + c_{55}k_z^2 - \lambda & (c_{13}+c_{55})k_xk_z \\ (c_{13}+c_{55})k_xk_z & c_{55}k_x^2 + c_{33}k_z^2 - \lambda \end{bmatrix} \begin{bmatrix} U_x \\ U_z \end{bmatrix} = 0. \tag{A-1}$$

The notations in Eq. A-1 has been declared above. Because the matrix of Eq. A-1 is positive, its determinant can be written as

$$det \begin{bmatrix} c_{11}k_x^2 + c_{55}k_z^2 - \lambda & (c_{13}+c_{55})k_xk_z \\ (c_{13}+c_{55})k_xk_z & c_{55}k_x^2 + c_{33}k_z^2 - \lambda \end{bmatrix} = 0, \tag{A-2}$$

From Eq. A-2 we can obtain a quadratic equation

$$a\lambda^2 + b\lambda + c = 0, \tag{A-3}$$

with

$$\begin{aligned} a &= 1, \\ b &= -[(c_{11}k_x^2 + c_{55}k_z^2) + (c_{55}k_x^2 + c_{33}k_z^2)], \\ c &= (c_{11}k_x^2 + c_{55}k_z^2)\cdot(c_{55}k_x^2 + c_{33}k_z^2) - (c_{13}+c_{55})^2k_x^2k_z^2. \end{aligned} \tag{A-4}$$

The discriminant of Eq. A-3 can be expressed as

$$\begin{aligned} \Delta &= b^2 - 4ac \\ &= [(c_{11}-c_{55})k_x^2 + (c_{55}-c_{33})k_z^2]^2 + 4(c_{55}+c_{13})^2k_x^2k_z^2 > 0. \end{aligned} \tag{A-5}$$

According to Eq. A-5, there are two real eigenvalues λ_1 and λ_2 for Eq. A-3 as

$$\begin{aligned} \lambda_{1,2} = &\frac{-b \pm \sqrt{b^2-4ac}}{2a} = \frac{(c_{11}+c_{55})k_x^2 + (c_{33}+c_{55})k_z^2}{2} \\ &\pm \frac{(c_{11}-c_{55})k_x^2 + (c_{33}-c_{55})k_z^2}{2} \\ &\cdot \sqrt{1 + \frac{4[(c_{11}-c_{55})(c_{55}-c_{33}) + (c_{13}+c_{55})^2]k_x^2k_z^2}{[(c_{11}-c_{55})k_x^2 + (c_{33}-c_{55})k_z^2]^2}}. \end{aligned} \tag{A-6}$$

Replacing the stiffness coefficients of Eq. (A-6) with elastic and anisotropic parameters as

$$\begin{aligned} \lambda_{1,2} = &\rho\frac{[(1+2\varepsilon)v_p^2 + v_s^2]k_x^2 + [v_p^2 + v_s^2]k_z^2}{2} \\ &\pm \rho\frac{[(1+2\varepsilon)v_p^2 - v_s^2]k_x^2 + [v_p^2 - v_s^2]k_z^2}{2} \\ &\cdot \sqrt{1 + \frac{8(\delta-\varepsilon)v_p^2(v_p^2-v_s^2)k_x^2k_z^2}{[((1+2\varepsilon)v_p^2 - v_s^2)k_x^2 + (v_p^2-v_s^2)k_z^2]^2}}. \end{aligned} \tag{A-7}$$

based on the weak anisotropy assumption, we approximate the square root item of Eq. A-7 via a first-order Taylor expansion around $\delta = \varepsilon$:

$$\begin{aligned} &\sqrt{1 + \frac{8(\delta-\varepsilon)v_p^2(v_p^2-v_s^2)k_x^2k_z^2}{[((1+2\varepsilon)v_p^2 - v_s^2)k_x^2 + (v_p^2-v_s^2)k_z^2]^2}} \\ &= 1 + \frac{4(\delta-\varepsilon)v_p^2(v_p^2-v_s^2)k_x^2k_z^2}{[((1+2\varepsilon)v_p^2 - v_s^2)k_x^2 + (v_p^2-v_s^2)k_z^2]^2}. \end{aligned} \tag{A-8}$$

Due to the second complicated item in Eq. A-8 (after the "=") far less than 1, we exclude this part and obtain the approximate eigenvalues as

$$\begin{aligned} \lambda_1 &= \rho v_p^2[(1+2\varepsilon)k_x^2 + k_z^2], \\ \lambda_2 &= \rho v_s^2[k_x^2 + k_z^2]. \end{aligned} \tag{A-9}$$

Equation A-9 corresponds to the solution of the Christoffel equation under the elliptical VTI assumption ($\varepsilon = \delta$). The accuracy tests of this approximate solution can be found in Zhang et al. (2022).

Next, we expand Eq. A-1 to linear equation system as

$$\begin{aligned} (c_{11}k_x^2 + c_{55}k_z^2)U_x + (c_{13}+c_{55})k_xk_zU_z &= \lambda U_x, \\ (c_{13}+c_{55})k_xk_zU_x + (c_{55}k_x^2 + c_{33}k_z^2)U_z &= \lambda U_z. \end{aligned} \tag{A-10}$$

we substitute λ_1 and λ_2 into Eq. A-10 and obtain

$$\mathbf{U_1} = \begin{bmatrix} k_x \\ \dfrac{\sqrt{[(1+2\delta)v_p^2 - v_s^2][v_p^2 - v_s^2]}}{(1+2\varepsilon)v_p^2 - v_s^2}k_z \end{bmatrix}, \tag{A-11}$$

and

$$\mathbf{U_2} = \begin{bmatrix} \dfrac{\sqrt{[(1+2\delta)v_p^2 - v_s^2][v_p^2 - v_s^2]}}{(1+2\varepsilon)v_p^2 - v_s^2}k_z \\ -k_x \end{bmatrix}, \tag{A-12}$$

where $\mathbf{U_1}$ and $\mathbf{U_2}$ represent the qP- and qS-wave polarization (Tsvankin, 2012), which are always orthogonal in anisotropic media.

References

Aki, K., Richards, P., 2002. Quantitative Seismology. University Science Books.

Berryman, J.G., 1979. Long-wave elastic anisotropy in transversely isotropic media. Geophysics 44, 896–917. https://doi.org/10.1190/1.1440984.

Biondi, B., 2007a. Angle-domain common-image gathers from anisotropic migration. Geophysics 72, S81–S91. https://doi.org/10.1190/1.2430561.

Biondi, B., 2007b. Residual moveout in anisotropic angle-domain common-image gathers. Geophysics 72, S93–S103. https://doi.org/10.1190/1.2430562.

Biondi, B., Symes, W.W., 2004. Angle-domain common-image gathers for migration velocity analysis by wavefield-continuation imaging. Geophysics 69, 1283–1298. https://doi.org/10.1190/1.1801945.

Caldwell, J., 1999. Marine multicomponent seismology. Lead. Edge 18, 1274–1282. https://doi.org/10.1190/1.1438198.

Cheng, J., Fomel, S., 2014. Fast algorithms for elastic-wave-mode separation and vector decomposition using low-rank approximation for anisotropic media. Geophysics 79, C97–C110. https://doi.org/10.1190/geo2014–0032.1.

Crampin, S., 1977. A review of the effects of anisotropic layering on the propagation of seismic waves. Geophys. J. Int. 49, 9–27. https://doi.org/10.1111/j.1365–246X.1977.tb03698.x.

Dellinger, J., Etgen, J., 1990. Wave-field separation in two-dimensional anisotropic media. Geophysics 55, 914–919. https://doi.org/10.1190/1.1442906.

Dellinger, J.A., 1991. Anisotropic Seismic Wave Propagation. Stanford University, p. 69.

Duan, Y., Sava, P., 2015. Scalar imaging condition for elastic reverse time migration. Geophysics 80, S127–S136. https://doi.org/10.1190/geo2014–0453.1.

Granli, J.R., Arntsen, B., Sollid, A., Hilde, E., 1999. Imaging through gas-filled

sediments using marine shear-wave data. Geophysics 64, 1566. https://doi.org/10.1190/1.1444576.
Jousselin, P., Biondi, B., 2006. Residual Moveout in Anisotropic Angle-Domain Common-Image Gathers with Dipping Reflectors: SEG Technical Program Expanded Abstracts, vols. 224–228. https://library.seg.org/doi/abs/10.1190/1.2369984.
Liu, L., 2019. Improving seismic image using the common-horizon panel. Geophysics 84, S449–S458. https://doi.org/10.1190/geo2018–0656.1.
Liu, L., Vincent, E., Ji, X., Qin, F., Luo, Y., 2016. Imaging diffractors using wave-equation migration. Geophysics 81, S459–S468. https://doi.org/10.1190/geo2016–0029.1.
Lu, Y., Liu, Q., Zhang, J., Yang, K., Sun, H., 2019. Poynting and polarization vectors based wavefield decomposition and their application on elastic reverse time migration in 2d transversely isotropic media. Geophys. Prospect. 67, 1296–1311. https://doi.org/10.1111/1365–2478.12777.
Morse, P.M., Feshbach, H., 1953. Methods of Theoretical Physics. McGraw-Hill Book Company.
Mu, X., Huang, J., Yang, J., Guo, X., Guo, Y., 2020a. Least-squares reverse time migration in tti media using a pure qp-wave equation. Geophysics 85, S199–S216.
Mu, X., Huang, J., Yong, P., Huang, J., Guo, X., Liu, D., Hu, Z., 2020b. Modeling of pure qp- and qsv-waves in tilted transversely isotropic media with the optimal quadratic approximation. Geophysics 85, C71–C89.
Qu, Y., Guan, Z., Li, Z., 2019. Topographic elastic least-squares reverse time migration based on vector p- and s-wave equations in the curvilinear coordinates. Geophys. Prospect. 67, 1271–1295.
Qu, Y., Huang, J., Li, Z., Guan, Z., Li, J., 2017a. Attenuation compensation in anisotropic least-squares reverse time migration. Geophysics 82, S411–S423.
Qu, Y., Li, Z., Huang, J., Li, J., 2017b. Viscoacoustic anisotropic full waveform inversion. J. Appl. Geophys. 136, 484–497.
Qu, Y., Zhu, J., Chen, Z., Huang, C., Wang, Y., Liu, C., 2022. Q-compensated least-squares reverse time migration with velocity-anisotropy correction based on the first-order velocity-pressure equations. Geophysics 1–71, 0.
Ruger, A., 1997. P-wave reflection coefficients for transversely isotropic models with vertical and horizontal axis of symmetry. Geophysics 62, 713–722. https://doi.org/10.1190/1.1444181.
Sava, P., Fomel, S., 2005. Wave-equation Common-Angle Gathers for Converted Waves, pp. 947–950. https://library.seg.org/doi/abs/10.1190/1.2148317.
Tang, C., McMechan, G.A., 2018. The dynamically correct poynting vector formulation for acoustic media with application in calculating multidirectional propagation vectors to produce angle gathers from reverse time migration. Geophysics 83, S365–S374. https://doi.org/10.1190/geo2017–0331.1.
Tang, J., Yue, H., Xiangrong, X., Tinnin, J., Hallin, J., 2009. Application of converted-wave 3d/3-c data for fracture detection in a deep tight-gas reservoir. Lead. Edge 28, 826–837. https://doi.org/10.1190/1.3167785.
Thomsen, L., 1986. Weak elastic anisotropy. Geophysics 51, 1954–1966. https://doi.org/10.1190/1.1442051.
>
Tsvankin, I., 2012. Seismic Signatures and Analysis of Reflection Data in Anisotropic Media, third ed. Society of Exploration Geophysics. https://doi.org/10.1190/1.9781560803003.
Vyas, M., Mobley, E., Nichols, D., Perdomo, J., 2010. Angle Gathers for Rtm Using Extended Imaging Conditions: SEG Technical Program Expanded Abstracts 2010, pp. 3252–3256. https://library.seg.org/doi/abs/10.1190/1.3513523.
Wang, C., Cheng, J., Arntsen, B., 2016a. Scalar and vector imaging based on wave mode decoupling for elastic reverse time migration in isotropic and transversely isotropic media. Geophysics 81, S383–S398. https://doi.org/10.1190/geo2015–0704.1.
Wang, W., McMechan, G.A., Tang, C., Xie, F., 2016b. Up/down and p/s decompositions of elastic wavefields using complex seismic traces with applications to calculating poynting vectors and angle-domain common-image gathers from reverse time migrations. Geophysics 81, S181–S194. https://doi.org/10.1190/geo2015–0456.1.
Wang, W., McMechan, G.A., Zhang, Q., 2015. Comparison of two algorithms for isotropic elastic p and s vector decomposition. Geophysics 80, T147–T160.
Wang, X., Zhang, J., 2022. Fast wave-mode separation in anisotropic elastic reverse time migration using the phase velocity-related poynting vector. J. Comput. Phys. 111200. https://doi.org/10.1016/j.jcp.2022.111200.
Xu, S., Zhang, Y., Tang, B., 2011. 3d angle gathers from reverse time migration. Geophysics 76, S77–S92. https://doi.org/10.1190/1.3536527.
Yan, J., Sava, P., 2008. Isotropic angle-domain elastic reverse-time migration. Geophysics 73, S229–S239. https://doi.org/10.1190/1.2981241.
Yan, J., 2009. Elastic wave-mode separation for vti media. Geophysics 74, WB19–WB32. https://doi.org/10.1190/1.3184014.
Yang, J., Zhang, H., Zhao, Y., Zhu, H., 2019. Elastic wavefield separation in anisotropic media based on eigenform analysis and its application in reverse-time migration. Geophys. J. Int. 217, 1290–1313. https://doi.org/10.1093/gji/ggz085.
Yang, J., Zhu, H., Wang, W., Zhao, Y., Zhang, H., 2018. Isotropic elastic reverse time migration using the phase- and amplitude-corrected vector p- and s-wavefields. Geophysics 83, S489–S503. https://doi.org/10.1190/geo2018–0023.1.
Zhang, D., Fei, T.W., Luo, Y., Tsingas, C., 2018. Rtm Angle Gathers by Optical Flow with Wavefield Separation: SEG Technical Program Expanded Abstracts, pp. 4387–4391. https://library.seg.org/doi/abs/10.1190/segam2018-2991159.1.
Zhang, L., Liu, L., Niu, F., Zuo, J., Shuai, D., Jia, W., Zhao, Y., 2022. A novel and efficient engine for p/s wave-mode vector decomposition for vti elastic reverse time migration. Geophysics 87, S185–S207. https://doi.org/10.1190/geo2021–0609.1.
Zhang, Q., Mcmechan, G.A., 2010. 2d and 3d elastic wavefield vector decomposition in the wavenumber domain for vti media. Geophysics 75, D13–D26. https://doi.org/10.1190/1.3431045.
Zhang, Q., Mcmechan, G.A., 2011a. Common-image gathers in the incident phase-angle domain from reverse time migration in 2d elastic vti media. Geophysics 76, S197–S206. https://doi.org/10.1190/geo2011–0015.1.
Zhang, Q., Mcmechan, G.A., 2011b. Direct vector-field method to obtain angle-domain common-image gathers from isotropic acoustic and elastic reverse time migration. Geophysics 76, WB135–WB149. https://doi.org/10.1190/geo2010–0314.1.
Zhang, Y., Biondi, B., Tang, Y., 2012. Residual Moveout-Based Wave-Equation Migration Velocity Analysis: SEG Technical Program Expanded Abstracts, pp. 1–5. https://library.seg.org/doi/abs/10.1190/segam2012-0332.1.
Zhao, Y., Liu, T., Jia, X., Liu, H., Xue, Z., Zhang, H.J., Zhu, H., Liang, H., 2020. Surface-offset gathers from elastic reverse time migration and velocity analysis. Geophysics 85, S47–S64. https://doi.org/10.1190/geo2018–0676.1.
Zhao, Y., Niu, F.L., Fu, L., Cheng, C., Chen, J.H., Huo, S.D., 2021. Local events-based fast rtm surface-offset gathers via dip-guided interpolation. Petrol. Sci. 18, 773–782. https://doi.org/10.1007/s12182–021–00557–y.
Zhao, Y., Zhang, H., Yang, J., Fei, T., 2018. Reducing artifacts of elastic reverse time migration by the deprimary technique. Geophysics 83, S569–S577. https://doi.org/10.1190/geo2018–0260.1.
Zhou, L., Chen, Z.C., Li, J.Y., Chen, X.H., Liu, X.Y., Liao, J.P., 2020. Nonlinear amplitude versus angle inversion for transversely isotropic media with vertical symmetry axis using new weak anisotropy approximation equations. Petrol. Sci. 17, 628–644. https://doi.org/10.1007/s12182–020–00445–x.
Zhu, H., 2017. Elastic wavefield separation based on the helmholtz decomposition. Geophysics 82, S173–S183. https://doi.org/10.1190/geo2016–0419.1.